RSC Advances

PAPER

View Article Online
View Journal | View Issue

Cite this: *RSC Adv.*, 2017, **7**, 36833

A nanocrystalline Co_3O_4@polypyrrole/MWCNT hybrid nanocomposite for high performance electrochemical supercapacitors

Sivalingam Ramesh,[a] Yuvaraj Haldorai,[b] Heung Soo Kim*[a] and Joo-Hyung Kim*[c]

In this study, a ternary hybrid nanocomposite of Co_3O_4@polypyrrole/MWCNT was prepared *via* oxidative polymerization of pyrrole monomer and a hybrid composite by a hydrothermal process. The synthesized hybrid nanocomposite was characterized by Raman spectroscopy, X-ray diffraction (XRD), X-ray photoelectron spectroscopy (XPS), scanning electron microscopy-EDX (SEM-EDX), and field emission resolution transmission electron microscopy (FE-TEM). The results of the structural and morphological studies of the hybrid nanocomposite show its controlled morphology and thermal stability. In addition, the electrochemical performances of charge–discharge cycles and impedance results were evaluated by cyclic voltammetry (CV) analysis. The as-synthesized hybrid nanocomposite was used to fabricate a three-electrode system in the presence of an electrochemical cell with 6 M potassium hydroxide (KOH) as electrolyte. The electrochemical performance of the hybrid composite displays good capacitive behavior with a specific capacitance of 609 F g^{-1} at a current density of 3 A g^{-1}, energy density 84.58 (W h kg^{-1}), power density 1500 (W kg^{-1}), and a good specific capacitance retention of *ca.* 97.1% after 5000 continuous charge–discharge cycles, indicating that the hybrid nanocomposite can be a promising electroactive material for supercapacitors.

Received 1st June 2017
Accepted 19th July 2017

DOI: 10.1039/c7ra06093a

rsc.li/rsc-advances

1. Introduction

Supercapacitors are an emerging energy storage nanotechnology that are attractive primarily due to their ability to store and release energy instantaneously, low cost, long life, and high power density of the materials.[1–3] This kind of energy power supply is predominately required for electric vehicles, consumer electronics, and portable devices.[4,5] The good features of high specific power density, fast charge and discharge rate, and long cycle life, mean that supercapacitors are recognized as important electrical energy storage materials. In electrochemical systems, the different energy storage mechanisms of supercapacitors can be classified into two categories: double-layer capacitors (EDLCs), and electrochemical pseudocapacitors (EPCs). The capacitance of EDLCs is based on charge separation at the electrode/electrolyte interface, and the capacitance of EPCs arises from fast and reversible faradic redox reactions that can occur within the electroactive materials.[6,7] Metal oxides play a very important role in many research fields of chemistry, physics, materials science and engineering, because due to the metal, a large diversity of metal oxides are able to be formed. Nanotechnology is utilized in the metal oxides for the fabrication of supercapacitors, sensors, microelectronic circuits, piezoelectric devices, and fuel cells.[8,9] The development of high performance electrode materials for supercapacitors has been of great interest in recent years, with reports on conducting polymers and carbon-based metal oxides.[10,11] One major part of the current research on supercapacitors is focused on fabricating better electrode materials with higher energy storage capacity, as well as lower fabrication costs and easily processable techniques.[12–14] Among the metal oxide materials, Co_3O_4 has attracted wide interest due to its high theoretical capacity, which meets the requirements for energy storage in the supercapacitors. However, its application is limited by the poor cyclability, resulting from its large volume expansion/contraction during electrochemical reactions. Many binary metal oxides, such as Co_3O_4, RuO_2, NiO, Mo_2O_3, V_2O_5 and MnO_2, showed promising performances in the ternary or higher order metal oxides for supercapacitor applications.[13–15] In particular, cobalt oxide (Co_3O_4) is a transition metal oxide with fascinating electronic, optical, electrochemical, and electrocatalytic properties of hybrid nanocomposites. The cobalt oxides and hydroxides proved that the much higher capacitance of the nanostructure than their conventional bulk counterparts has significant effects on the capacitance performance of the active electrode materials. Cobalt oxide thin film has been synthesized by various methods, such as hydrothermal, spray

[a]*Department of Mechanical, Robotics and Energy Engineering, Dongguk University – Seoul, Pil-dong, Jung-gu, 100-715 Seoul, South Korea. E-mail: heungsoo@dgu.edu*
[b]*Department of Energy Engineering, Dongguk University – Seoul, Pil-dong, Jung-gu, 100-715 Seoul, South Korea*
[c]*Department of Mechanical Engineering, Inha University, Inha-ro 100, Nam-gu, Incheon 402-751, South Korea. E-mail: joohyung.kim@inha.ac.kr*

pyrolysis, sputtering, chemical vapor deposition (CVD), pulse laser deposition, sol–gel process, and electrodeposition for different substrates materials.[16–18] The cobalt oxide (Co_3O_4)-based hybrid nanocomposites offer great potential in the field of supercapacitors, heterogeneous catalysts, electrochemical sensors, and Li–ion rechargeable batteries.[19] In addition, polypyrrole (PPy) has received attention for the easy oxidation, water solubility, and commercial availability of pyrrole monomers. PPy and carbon materials have attracted attention due to the synergistic effects between these carbon-based components. The conducting PPy shows unique properties in the doping mechanism, and high electrical conductivity due to the promising electrode materials in pseudo-capacitors. The electrical conductivity and control morphology of PPy may be very useful in the electrochemical performance of supercapacitors. The porous PPy showed good capacitance performance on hybrid composites and conducting pathways, effective interface area, and nanoscale dimensions. The composites, PPy as the matrix material, of a wide range of desirable properties have received tremendous research, as they have potential applications in many fields, such as molecular electronics, electrochemical display devices, catalysis, electromagnetic shields, microwave-absorbing materials, supercapacitors, and batteries.[20–22] Many studies have been performed in order to examine the redox properties of PPy synthesized in the presence of different electrolytes based on cyclic voltammetry measurements. Therefore, the PPy hybrid composites have also been synthesized by various active substrates, such as graphene, carbon nanotubes (CNTs), and graphene oxide, to increase the surface area and improve electrical conductivity. The CNT–PPy composites are reported in the specific capacitance range of 180–500 F g^{-1} in the hydrothermal process. In the graphene oxide, PPy composites have been synthesized by an *in situ* chemical polymerization, and show good performance with a specific capacitance of 728 F g^{-1} at a discharge current density of 0.5 A g^{-1}. The control morphology of Co_3O_4 nanotubes hybrid composite *via* micro emulsion, colloidal template method, template assisted, and direct oxidation of cobalt nanowires were reported in the literature.[20–22] Although many research articles have been published based on the synthesis of carbon nanotube/Co_3O_4 composites for supercapacitor properties, the fabrications of hybrid composite with attractive morphologies are scarce in the literature.[20–23] Therefore, the hybrid composites with different architectures are undoubtedly promising electrode materials for supercapacitors. In the present study, Co_3O_4@MWCNT/PPy hybrid composites were synthesized by a hydrothermal process as electrode materials. Their supercapacitor behavior was investigated in 6 M L^{-1} KOH electrolyte solution by cyclic voltammetry (CV), galvanostatic charge–discharge tests, and electrochemical impedance spectroscopy analysis (EIS).

2. Experimental section

2.1. Materials

All chemicals reagents were of analytical grade, and were used without any further purification process. The multiwall carbon nanotube (MWCNT-CMP-310F, MWCNT 10–20 nm) purchase from ILjin Nanotech Co. Ltd, South Korea. Pyrrole, sulphuric acid, nitric acid, ferric chloride ($FeCl_3$), sodium dodecyl benzenesulfonate (SDBS), butanol, hexane and cobalt chloride, potassium hydroxide (KOH) and polytetrafluorethylene (PTFE) were used in the present study as received from Aldrich Chemical Company, South Korea.

2.2. Synthesis of carboxylic group's functionalization

MWCNTs were synthesized by oxidation according to the reported procedure.[23,24] The calculated amounts of 0.5 g of MWCNTs were dispersed in 80 mL of concentrated H_2SO_4 and HNO_3 with a volume ratio of 3 : 1, using an ultrasonicator for 1 h. The reaction mixture was heated at 80 °C for 6 h, and washed with water several times, until becoming a neutral pH = 7. The resultant product of the functionalized MWCNTs was filtered by using 0.2 μm PTFE membrane filter, and dried in vacuum at 80 °C for 24 h. Finally, the carboxylic functionalized multiwall carbon nanotubes materials underwent further characterization.

2.3. Synthesis of polypyrrole (PPy)–MWCNT hybrid composite

The chemical composition of the microemulsion process of PPy–MWCNT hybrid nanocomposite system was followed by the Santhosh Paul process.[25] The micro emulsion protocol (Fig. 1) was as follows: 0.5 g ferric chloride ($FeCl_3$), 20 mL of distilled water, 4 g sodium dodecyl benzenesulfonate (SDBS), 0.9 mL of butanol, and 6 mL hexane were used. The PPy–MWCNT hybrid composite was synthesized *via in situ* microemulsion polymerization, where the calculated amount of pyrrole and 0.5 g of $FeCl_3$ was added slowly to initiate the polymerization of PPy monomer. Then, the MWCNTs were dispersed into the microemulsion system containing monomer by sonication, and then underwent constant stirring at 90 °C for 12 h. The polymerization reaction system was quite stable, without any evident precipitation. Finally, the reaction mixture was filtrated, and washed with ethanol and water several times, and the resultant black powder was dried in vacuum at 90 °C for 24 h. The purified product of PPy–MWCNT hybrid composite was collected for further analysis in a sealed bottle to avoid moisture.

2.4. Synthesis of Co_3O_4@PPy/MWCNT hybrid composite

The cobalt oxide was synthesized from cobalt chloride, 0.5 g of PPy–MWCNT, and 7.25 g of cobalt chloride in 50 mL of distilled water and vigorous stirring at 90 °C for 3 h. The PPY–MWCNT and cobalt chloride were mixed together, and were well dispersed in the presence of water. After that, the required amount of 25% ammonia was added in dropwise, controlled to basic pH = 9, and continuously stirred for 12 h. The reaction mixture was then filtered and dried in vacuum oven at 90 °C for 6 h, and washed with ethanol, and next, the product of cobalt hydroxide underwent calcination at 180 °C for 12 h. The resultant product of cobalt oxide was purified by ethanol several times, and the sample collected for further characterization in sealed bottle.

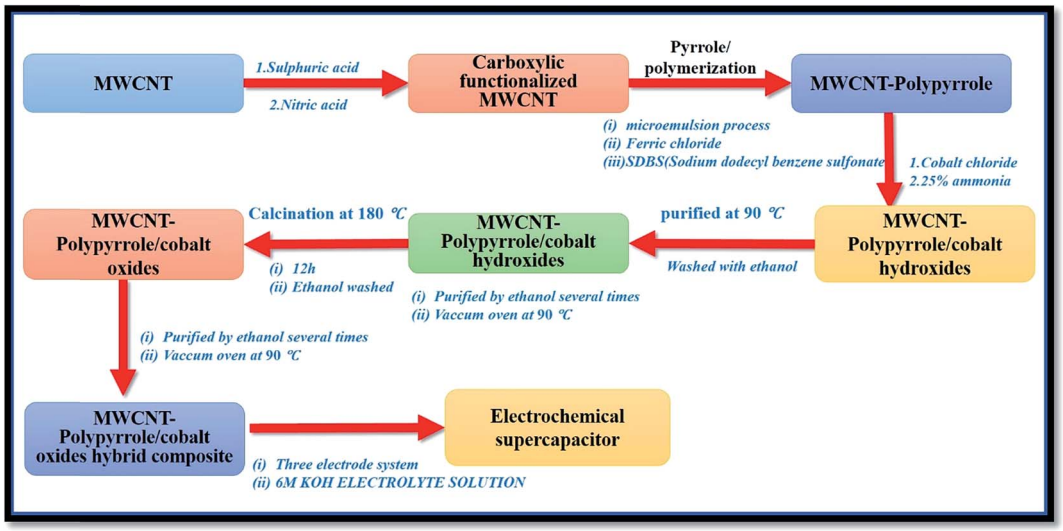

Fig. 1 Step-wise synthesis of Co_3O_4/MWCNT/PPy hybrid composite.

2.5. Electrochemical analysis

The electrochemical performance tests were characterized by using a three-electrode system. This electrochemical system contained Pt electrode, Ag/AgCl electrode, and working electrode (Co_3O_4@PPy/MWCNT). In this test, we performed cyclic voltammetry (CV), chronopotentiometry (CP), and electrochemical impedance spectroscopy (EIS). The electrochemical results were obtained on an (Autolab PGSTAT302N Metrohm, Netherlands) electrochemical workstation at room temperature, followed by CV analysis for the use of 6 M KOH solution as electrolyte. The electrode preparation and electrochemical characterization were conducted according to the following steps. The active materials of 75 wt% (hybrid composite), 20 wt% acetylene black as a conducting agent, and 5 wt% polytetrafluorethylene (PTFE) as a binder, were mixed to a homogenous state, and pressed into a nickel foam (1 cm × 1 cm) current collector under a pressure of 8 MPa. Based on the composition, the electrochemical measurements were carried out at room temperature in a three-electrode system consisting of the electrode as hybrid composite working electrode, an Ag/AgCl as reference electrode, and a platinum wire as counter electrode, in the presence of 6 mol L^{-1} KOH electrolytic solution. The electrochemical behavior of the hybrid electrode was characterized by cyclic voltammetry (CV), galvanostatic charge–discharge tests, and electrochemical impedance spectroscopy test at a Versa STAT3 electrochemical workstation (Princeton Applied Research, USA). The CV was conducted in the potential range between 0.0 and 0.10 V *versus* SCE at various scan rates. The constant current charge–discharge test was carried out at different current densities in the potential range of −0.1 to 0.0 V. Electrochemical impedance spectroscopy was carried out to prove the capacitive performance at open circuit potential in 6 M L^{-1} KOH in the frequency range of 0.01–105 Hz.

2.6. Characterization

FTIR spectra were obtained by Bio-Rad FTS 3000 spectrometry from Digilab (Cambridge, USA) with KBr beam splitter, detector at 8 cm^{-1} resolution, and 300 scans per sample. Wide-angle XRD patterns of hybrid composite samples were recorded by Rigaku Rotaflex (RU-200B) X-ray diffractometry using Cu-K_α radiation with a Ni filter. The tube current and voltage were 300 mA and 40 kV, respectively, and data from the 2θ angular regions between 5 and 80 °C were collected. The morphology, size, and structure of the materials were determined by field-emission scanning electron microscopy (FE-SEM, Hitachi S-4800, Japan), and high-resolution TEM (HR-TEM, JEM-2010F). The amount of cobalt present in the hybrid composite was studied by inductively coupled plasma mass spectrometer (ICP-MS-Elan6100/Perkin Elmer, Frequency-40 MHz detection limit range – sub ppb). The hybrid composite samples were characterized by using particle size analyzer (Mastersizer 2000/Malvern) the size range from (0.02−2000 μm), light sources-(Red He–Ne, laser 633 nm) and (Blue solid state light source 466 nm, power 110/240 V) Worcestershire, UK. The surface properties were characterized by physisorption analyzer (ASAP2020/micromeritics), surface area 0.0005 m^2, temperature 1100 °C and ramp rate from 1−20 °C min^{-1} Atlanta, GA. The electrochemical properties were studied by means of cyclic voltammetry (CV) analysis. In this experiment, three-electrode systems were used, such as working electrode (hybrid composite), Ag/AgCl as the reference electrode, and Pt wire as the counter electrode. The CV was scanned from −0.1 to 0.0. SCE at a series of scan rates ranging from 100 to 10 mV s^{-1}. The galvanostatic charge discharge (GCD) was performed at current densities from 1 to 15 A g^{-1}, and impedance spectroscopy (EIS) was carried out in the frequency range of range of 0.01–105 Hz amplitude, referring to the open circuit potential.

3. Results and discussion

3.1. FTIR spectral analysis

The FT-IR spectra recorded for PPy, MWCNT, and PPy–MWCNT hybrid composite nanocomposite results were discussed in detail.[26] In the FT-IR spectrum of MWCNT, the small intense

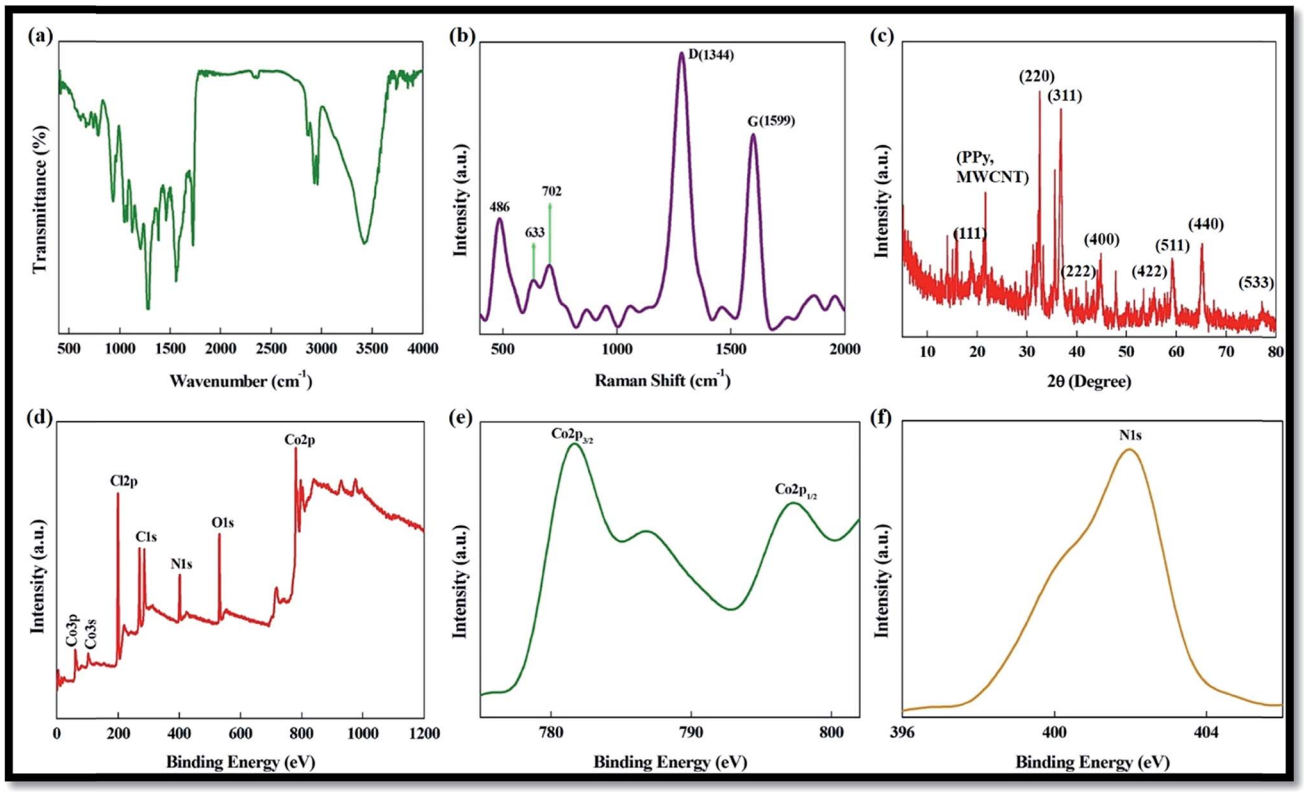

Fig. 2 (a) FTIR, (b) Raman, (c) XRD patterns, (d) survey XPS, (e) individual Co 2p, and (f) N 1s spectral results of the Co_3O_4/MWCNT/PPy hybrid composite.

peaks of 1687 and 1728 cm^{-1} correspond to the C=C stretching and C=O stretching vibrations of the carboxylic group, respectively, indicating that the MWCNTs had been successfully oxidized into carboxylate carbon nanotubes. Fig. 2(a) represents the FTIR spectral results of PPy–MWCNT and hybrid composite, in which the absorption bands that occurred at 1560 cm^{-1} and 1429–1497 cm^{-1} represent the anti-symmetric, and symmetric and anti-symmetric C–C stretching vibration of pyrrole ring structure, respectively. The band at 1357 cm^{-1} is related to the C–N in-plane, and the bands at 1286, 1236, 1151 and 1093 cm^{-1} are associated with the C–H bending modes, while the band for C–H out-of-plane deformation vibration was observed at 987–665 cm^{-1}. It was observed that all the spectra contain a very weak but broad adsorption band in the region between 2927–3425 cm^{-1}, which is confirmed for the adsorption band of O–H, C–H, and N–H groups. The characteristic peaks of PPy at 1454 cm^{-1} and 1558 cm^{-1} that are also observed for the PPy–MWCNT composites represent the formation of PPy in the presence of MWCNT. It is important to observe that the peak of PPy at 1560 cm^{-1} broadens slightly in almost all hybrid composite samples, and the characteristic peaks of MWNTs are hardly seen, which indicates better interaction between the aromatic ring of pyrrole and MWCNT. However, the incorporation of MWCNT results in the slight shifting of FT-IR peaks from their original positions. These shifts in the peak positions are due to the strong synergetic interaction between the PPy and MWCNTs.[26] Furthermore, the broad bands centered around 1689 and 3429 cm^{-1} are assigned to O–H stretching and bending modes of water, respectively. The absorption peaks at 661 and 573 cm^{-1} represent the Co–O modes from cobalt oxide, and the peak at 3012–3423 cm^{-1} can be related to N–H stretching vibrations in the hybrid composite.[14,19,26]

3.2. Raman spectral results

Fig. 2(b) shows the Raman spectrum of the pristine PPy. The characteristics bands appearing at 1572 and 1337 cm^{-1} were assigned to the C=C backbone stretching and ring stretching vibration of PPy, respectively. Raman spectrum of the carboxylated MWCNTs showed two prominent characteristics peaks of D-band (1344 cm^{-1}) and G-band (1599 cm^{-1}). In the PPy–MWCNT hybrid composite, the D-band becomes broad, and in the G-band of MWCNTs, (C=C) stretching vibrations are merged into a broad band, with a maximum at 1579 cm^{-1}. In addition, when MWCNT was introduced into the PPy matrix, both these D- and G-bands shifted slightly. This is probably due to the doping of the carboxyl group of functionalized MWCNTs to PPy backbone, and π–π interaction between PPy and MWCNTs. The Raman spectra of the pristine PPy, MWCNT and PPy–MWCNT nanocomposite results were discussed in detail,[27] and in Fig. 2(b), show three main bands at 486, 633 and 702 cm^{-1}. These bands represent the crystalline Co_3O_4, namely the E_g, F_{2g}, and A_{1g} modes, respectively. In addition, the D- and G-bands at 1344 and 1599 cm^{-1}, respectively, confirmed the presence of MWCNT hybrid composite. The D-band is usually

related to the breathing mode of rings, while the G-band represents the sp^2 hybridized carbon atoms.

3.3. X-ray diffraction analysis (XRD)

Zhang *et al.*[27] shows the XRD pattern of PPy, PPy–MWCNT hybrid nanocomposite. The diffraction peaks of MWCNT–PPy indicate the formation of PPy–MWCNT hybrid composite by an *in situ* polymerization process.[27] The spectral result shows the peak at $2\theta = 22.36°$ to 28.30° can be attributed to the MWCNT–PPy structure. In addition, Fig. 2(c) shows the PPy–MWCNT/cobalt oxide hybrid nanocomposite results. The diffraction peaks at 5.14°, 13.98°, 15.84°, 18.7°, 21.68° (PPy–MWCNT), 32.56°, 35.62°, 35.86°, 39.92°, 41.9°, 44.86°, 47.88°, 36.8°, 38.9°, 44.8°, 53.46°, 55.14°, 59.22°, 65.24°, 67.60°, and 77.4° can be denoted as (111), (220), (311), (222), (400), (422), (511), (440), and (533) reflections, respectively, of the face-centered cubic structure of Co_3O_4. The peak at 21.68° corresponds to the (002) reflection of MWCNT.[28–30] Therefore, the synthesized $Co(OH)_2$ can be transformed to Co_3O_4 by calcination at 180 °C. After being annealed at 180 °C for 1 h in air, the synthesized $Co(OH)_2$ crystals were completely converted to pure spinel Co_3O_4 in the hybrid composite. It can be seen that all the diffraction patterns can be readily assigned to the cubic structure of Co_3O_4 (JCPDS card, 42-1467). The broadening peaks indicate that the crystal size of Co_3O_4 is small, and there are no impurities. This results indicate the complete transformation of $Co(OH)_2$ into Co_3O_4 by the calcination process, in which the change of color of the compound from pink to black indicates the phase transformation. This color change represents the oxidation from Co(II) to Co(III) oxide by atmospheric oxygen.

3.4. X-ray photoelectron spectroscopy (XPS)

XPS was performed in order to deeply characterize the elemental composition of the surface of the hybrid composite, as well as the chemical environment of the cobalt, oxygen and carbon atoms. Fig. 2(d) shows the high-resolution spectral results for the cobalt oxides (Co 2p, O 1s and C 1s) core levels, respectively. The survey XPS spectrum (Fig. 2(d)) of the hybrid composite shows C 1s (283.4 eV), O 1s (530.4 eV), N 1s (397.8 eV), and Co 2p (780.7 eV), which confirms the presence of these elements in the composite. Fig. 2(e) shows that the spin–orbit peaks in the high-resolution spectrum for Co $2p_{3/2}$ and Co $2p_{1/2}$ are observed at 780.7 and 796.5 eV, respectively, which are in good agreement with the previous studies.[28–30] The core-level N 1s spectrum (Fig. 2(f)) result shows that the 398–402.2 eV corresponds to PPy nitrogen.

3.5. Morphological and surface properties of the hybrid composite

Fig. 3 and 4(a)–(f) show FE–TEM imagery of the pristine MWCNTs and PPy/MWCNT hybrid composites. The average diameter of the pristine nanotubes was measured to be about 10–20 nm. These images of PPy/MWCNT composites all show the hybrid composites well dispersed in the carbon nanotubes enwrapped uniformly with PPy polymer. This suggests that the interaction between polymer molecules and MWCNTs overcomes the Van der Waals interaction between carbon nanotubes. Therefore, the morphology of the Co_3O_4 hybrid composite shows nanotubes of 10–20 nm size were dispersed on the MWCNT surface with polycrystalline behavior. The SAED pattern of the hybrid composite. Fig. 4(e) shows well-defined rings, which could be attributed to the crystalline nature of Co_3O_4. Fig. 4(f) illustrates EDS mapping images of the hybrid composite. In addition the particles distribution curves of MWCNT, Co_3O_4/MWCNT and Co_3O_4/MWCNT/PPy hybrid composite results are shown in Fig. 5. The surface properties of MWCNT and Co_3O_4/MWCNT/PPy hybrid composites are shown in Fig. 6 and 7. This results suggest that the hybrid composite showed control morphology and well decorated Co_3O_4 into MWCNT/PPy surface.

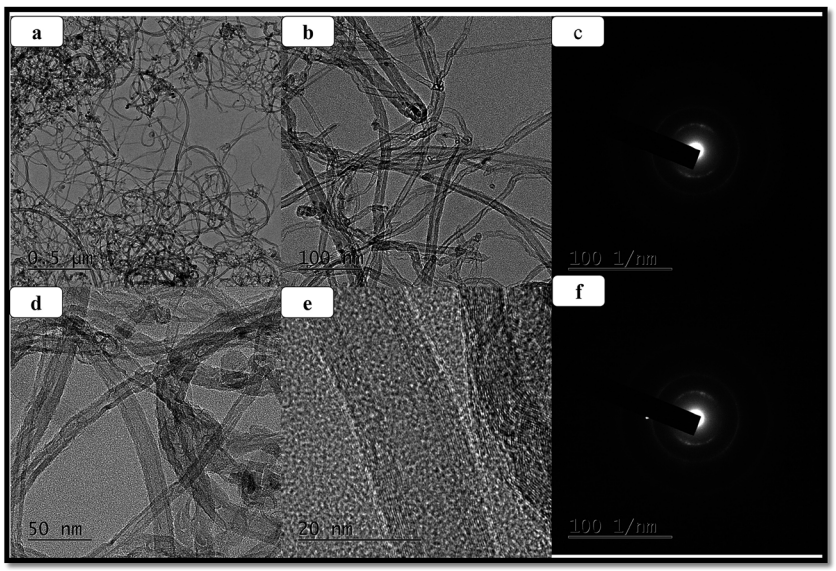

Fig. 3 Different magnification of TEM morphology of MWCNT (a–d) (e) FE-TEM, (f) SAED pattern of MWCNT.

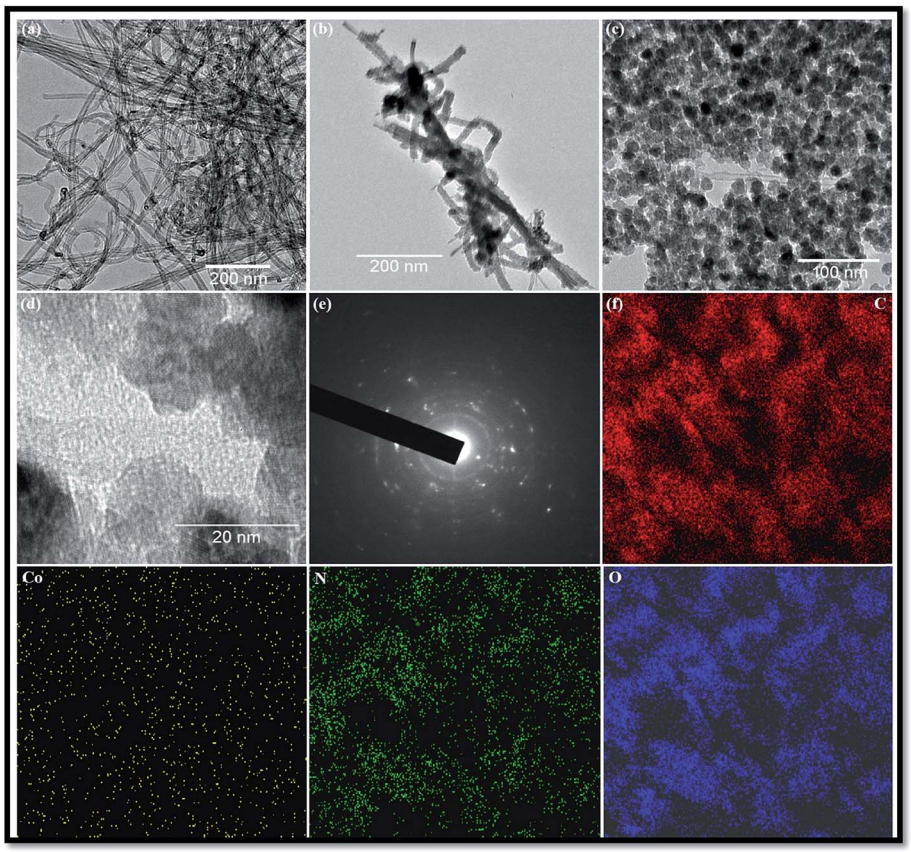

Fig. 4 (a) MWCNT, (b) and (c) TEM imagery (different magnification), (d) FE-TEM, (e) SAED pattern, and (f) EDS mapping of Co_3O_4/MWNT/PPy hybrid composite.

3.6. Cyclic voltammograms

Cyclic voltammetric measurements (CV) were performed in a potential range between −0.10 to 0.0 V (*versus* Ag/AgCl), to examine the electrochemical characteristics of the prepared hybrid composite. Fig. 8(a) presents the CV curves of the hybrid composite electrode in 6 M L^{-1} KOH at the scan rates of 10 to 100 mV s^{-1}. A pair of well-defined broad redox reaction peaks is visible in the CV curves, indicating that the electrochemical capacitance of the hybrid composite electrode mainly results from the pseudocapacitance. Furthermore, the peak current increases with increasing scan rate from 10 to 100 mV s^{-1}, which suggests its good reversibility of the fast charge–discharge response. The possible mechanism may be attributed to $Co_3O_4 + OH^- + H_2O \rightarrow 3CoOOH + e^-$. According to the literature,[31,32] the surface adsorption of high concentration alkali ions can decrease the electrolyte starvation near the electrode surface and reduce the internal resistance of the electrode, which factors help to improve the pseudocapacitance resulting from the above surface reaction. Fig. 8(a) shows the CVs that were conducted at a scan rate of 10–100 mV s^{-1} in 6 M KOH over the potential range of −0.1 to 0.0 V *versus* Ag/AgCl, for the Co_3O_4@MWCNT/PPy hybrid composite electrodes. The shape of the CV loop for the composite electrode shows well-defined broad redox reaction without any redox peaks, indicating a double layer capacity behavior. The electrode shows a higher current density response than the MWNT, indicating its good charge storage performance. These results suggest that the overall capacitance of the electrode increases, due to the presence of Co_3O_4. The CV tests of the electrode Fig. 8(a) at various scan rates (10, 20, 40, 60, 80, and 100 mV s^{-1}) shows well defined broad redox reaction indicating its good capacitance behavior. The specific capacitance of the hybrid electrode can be calculated according to the following equation.[31,32] The CV results of measured pseudocapacitance values are mainly depends on redox reactions between the cobalt oxide–MWCNT/PPy. As the scan rate increased, the overall shape of the curves was maintained, indicating good high-rate performance. The specific capacitances calculated from the CV curves are 615, 490, 383, 308, 295 and 276 F g^{-1} for scan rate of 10, 20, 40, 60, 80 and 100 mV s^{-1} respectively.

3.7. Galvanostatic charge–discharge analysis

The MWCNT have been attractive materials for electrodes of supercapacitors due to their high accessible surface area, high electronic conductivity, chemical and mechanical stability. The specific capacitance of pristine MWCNTs (90–140 F g^{-1}).[33,34] In order to improve the mechanical and electrochemical properties of electrodes based on conducting polymers, the composites of conducting polymers and CNTs have been synthesized for supercapacitor applications. It has been shown that CNTs

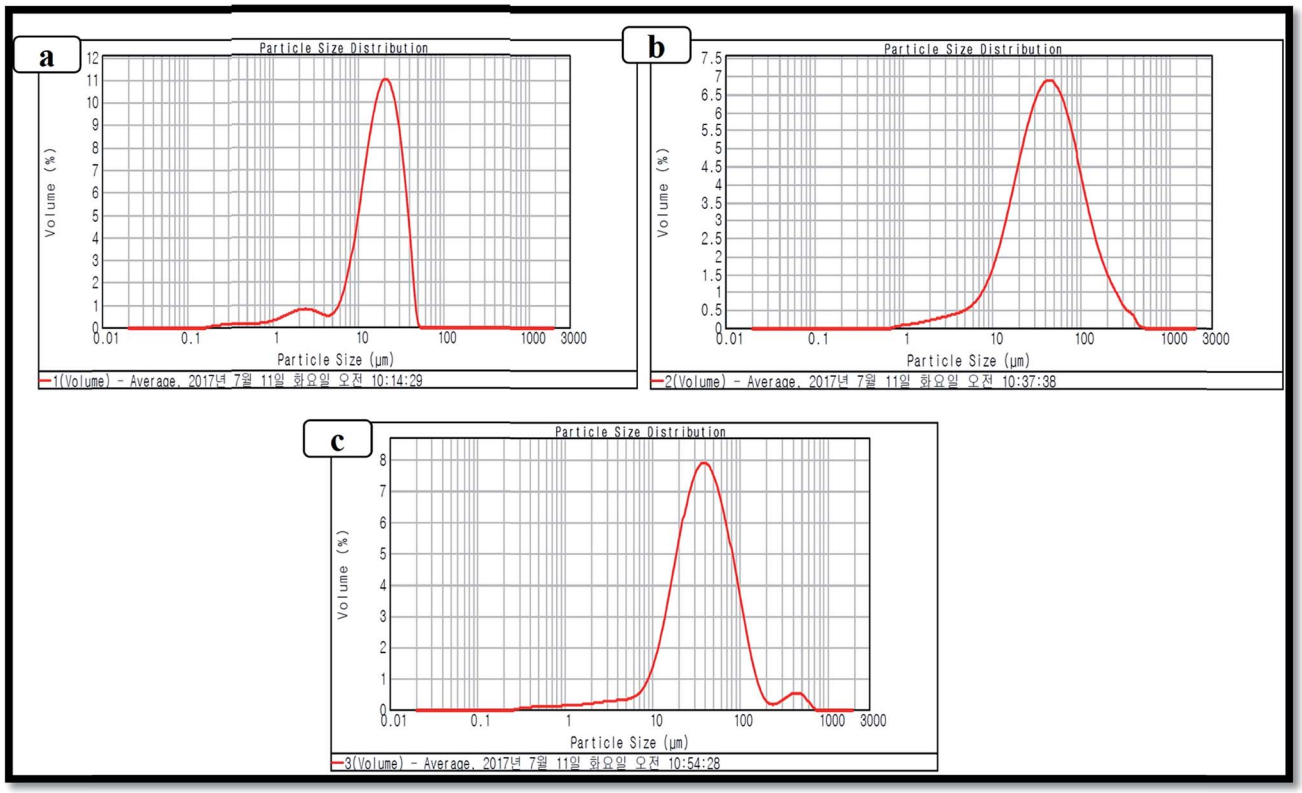

Fig. 5 Particles size distribution curves (a) pristine Co_3O_4 (b) Co_3O_4/MWCNT (c) Co_3O_4/MWCN/PPy hybrid composite.

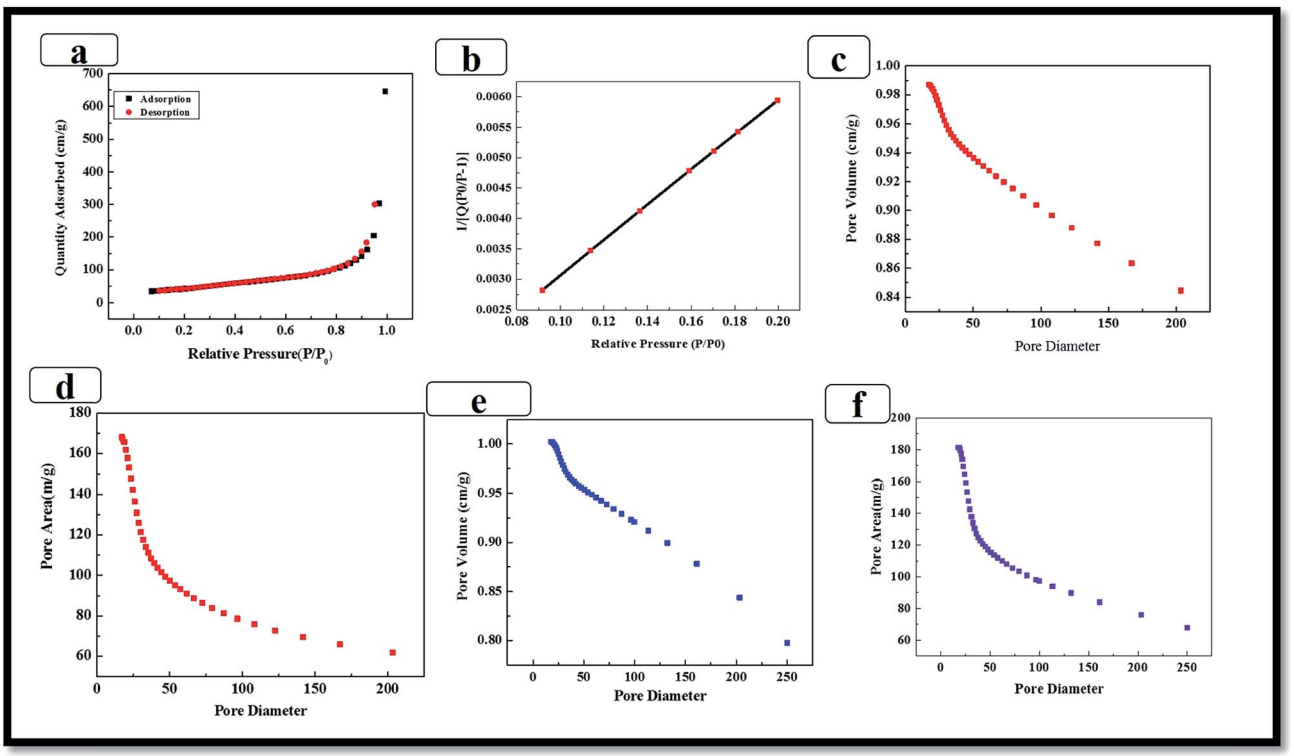

Fig. 6 (a–f) BET results of MWCNT composite.

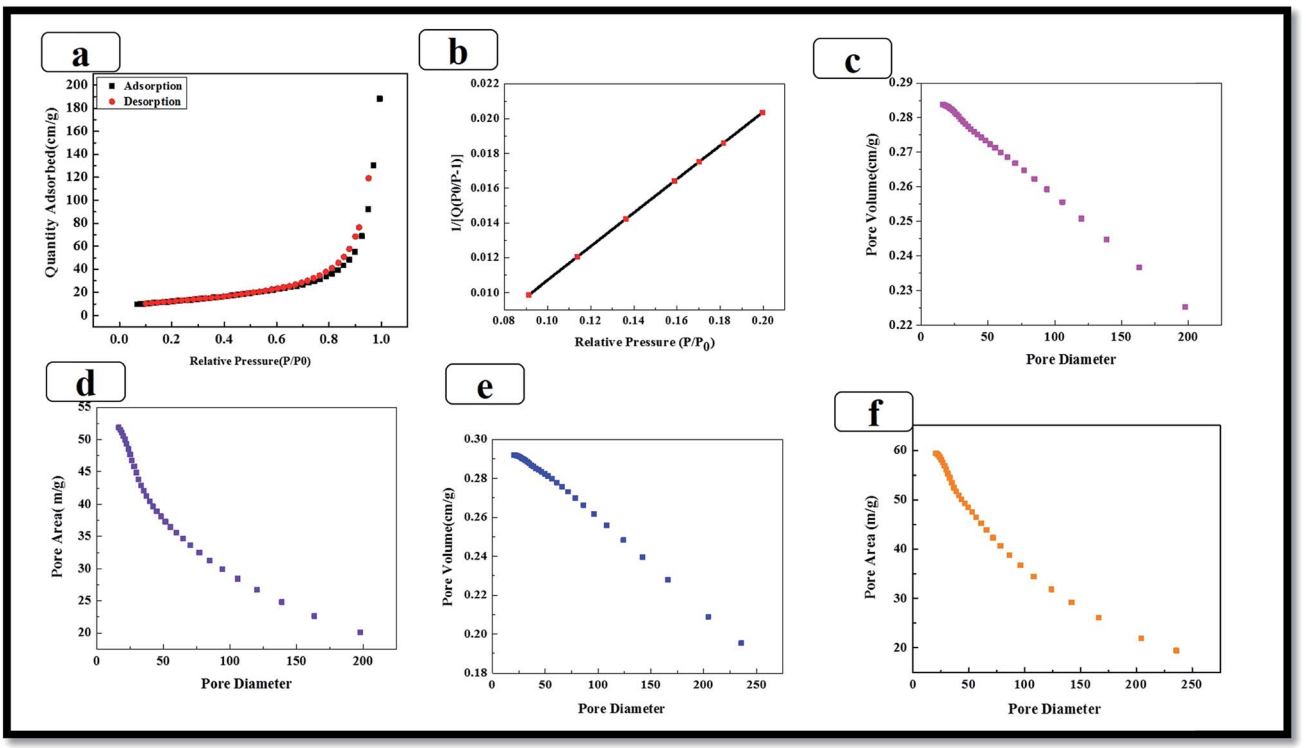

Fig. 7 BET results of Co_3O_4/MWCNT/PPy hybrid composite.

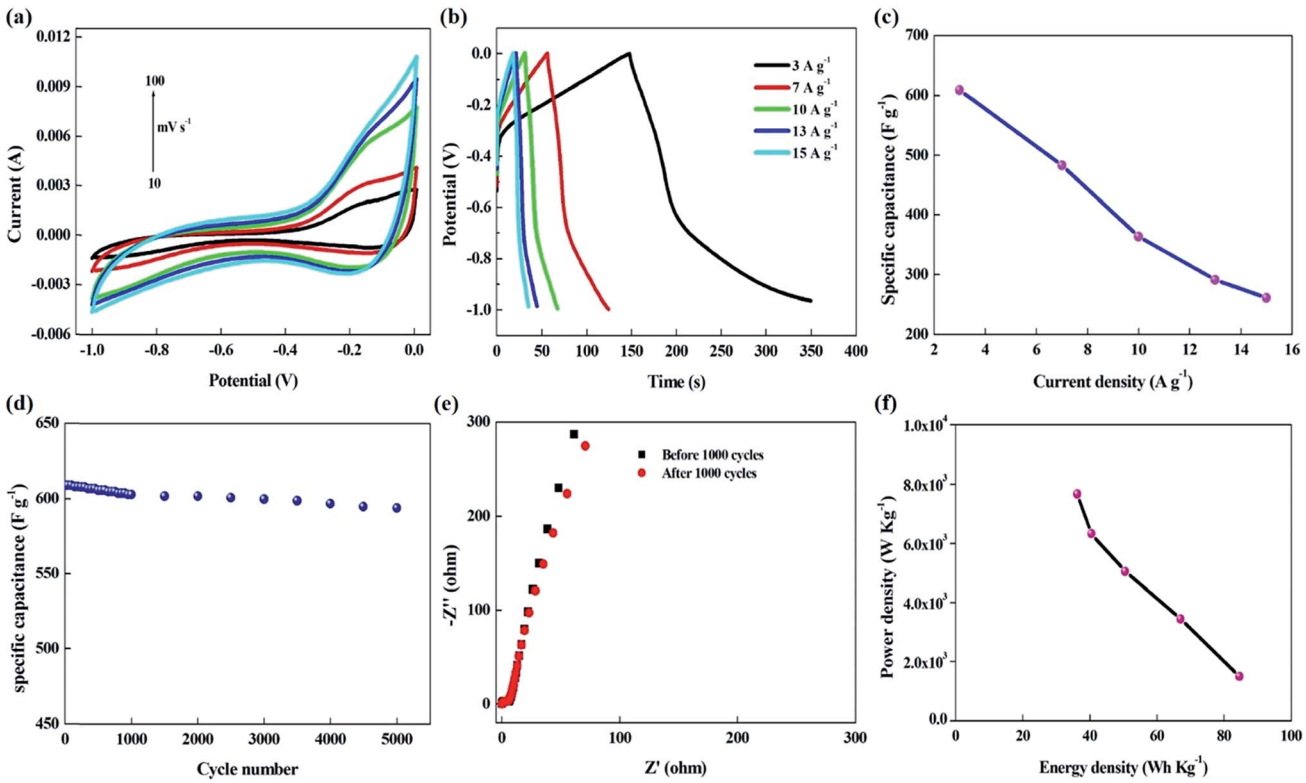

Fig. 8 (a) CVs of the Co_3O_4/MWNT/PPy hybrid composite electrodes in 6 M KOH at a scan rate of the electrode at various scan rates, (b) charge–discharge curves of the electrode at various current densities, (c) corresponding specific capacitance, (d) variation of specific capacitance as a function of cyclic number at a current density of 3.0 A g^{-1}, (e) Nyquist plots, and (f) power density of the hybrid electrode.

play a role of a perfect backbone for a homogeneous distribution of conducting polymer in the composites. In many studies, various nanostructured PPys, such as nanofibers, porous structures, and even films, have been synthesized and the specific capacitance ranged from 170 to 300 F g^{-1}. The PPy composites have also been synthesized by using various active substrates, such as carbon nanotubes (CNTs), graphene oxide, graphene, to increase the surface area and improve electrical conductivity. CNT–PPy composites are reported to have the specific capacitance of 180–500 F g^{-1}. The PPy grafted graphene nanosheet composites have been fabricated by the *in situ* chemical oxidative grafting polymerization, revealing a maximum discharge capacitance of 191.2 F g^{-1}. Kim *et al.* reported that high-specific capacitance and good high-rate capability of PPy/CNT composite electrodes in presence of three-dimensional entangled structure of a CNTs.[33–47] In addition, the chemical synthesis of free-standing PPy nanotubes provides a potential candidate for thermoelectric application and membrane for anode of microbial fuel cells. Based on these aspects it has been reported the use of CNTs materials in association with pseudocapacitors to achieve the desired performance for energy storage devices. The specific capacitance of PPy–MWCNT nanotube was reported 140–211 F g^{-1} depends on the morphology and surface area of the materials. The electrode was prepared through a facile and effective method, which combined the acid treatment of MWCNTs and *in situ* decomposition of $Co(NO_3)_2$ in *n*-hexanol solution at 140 °C. The MWCNTs/Co_3O_4 composites show high capacitor property, and their specific capacitance is up to 200–590 F g^{-1} at 1–15 A g^{-1}, which is significantly greater than that of pure MWCNTs (90 F g^{-1}). To increase the conductivity of the composites, different substrate materials can be adopted. The highly ordered inorganic nanotube array materials can be applied as substrate materials owing to their high surface area and chemical–electrochemical stability.[33–47]

Fig. 8(b) shows the initial five galvanostatic charge–discharge curves of the hybrid composite electrode in 6 M L^{-1} KOH solution at a galvanostatic current density of 3, 7, 10, 13, and 15 A g^{-1}. An approximately mirror-like potential-time response behavior can be observed, which also implies that the charge–discharge process of the hybrid composite electrode is reversible. The specific capacitance has been calculated from the following equation:[33–35] Fig. 8(c) shows the specific capacitance *versus* current density plot. The hybrid composite showed specific capacitances of 609, 483, 364, and 291 F g^{-1} at 3, 7, 10, 13, and 15 A g^{-1} respectively. The specific capacitance decreases as the applied current increases, due to the limited movement of electrolyte ions through the electrodes. The hybrid composite exhibits higher capacitance (609 F g^{-1}) than pure MWNT, due to the decoration of cobalt oxide onto the MWNT/PPy surface, which effectively prevents the agglomeration of MWNT, thereby facilitating ion transport in the electrode material, increasing the EDLC. Moreover, the composite shows a capacitance of 291 F g^{-1} even at a high current density of 15 A g^{-1}, indicating its excellent rate capability. Fig. 8(d) shows a plot of the cyclic number *versus* the specific capacitance. The electrode shows only 2.9% capacitance loss after 5000 cycles at a current density of 3 A g^{-1}, indicating its outstanding rate capability. This is attributed mainly to the good interconnectivity between the Co_3O_4 and MWNT/PPy, rapid electron transfer and charge separation, and good conductive network. Table 1 shows the comparison of our results with the previously reported hybrid composite electrodes. The specific capacitance of the hybrid composite electrode determined from the discharge curves is *ca.* 609 F g^{-1} at a current density of 3 A g^{-1}, which is much larger than that of the crater-like Co_3O_4 microspheres and mesoporous Co_3O_4 nanoparticles.[33–35] The outstanding electrochemical capacitance of the synthesized hybrid composite electrode can be attributed to its unique morphology and large specific surface area, which help to enlarge the contact area between electrode and electrolyte in the presence of 6 M KOH. The small capacitance fading at a very high galvanostatic current density shows that the hybrid composite structure allows for a rapid redox reaction at high current densities. Galvanostatic charge–discharge experiments were undertaken to study the cycling stability of the hybrid composite electrode. The charge–discharge studies were performed at a current density of 3 A g^{-1} in 6 M L^{-1} KOH solution, and Fig. 8(d) shows

Table 1 Comparison of the supercapacitor values of Co_3O_4@MWCNT/polypyrrole with other electrodes reported in the literature[a]

Electrode material	Capacitance (F g^{-1})	Cyclic stability	Ref.
Co_3O_4	118 F g^{-1} at 0.1 A g^{-1}	6.56% loss after 1000 cycles	39
Co_3O_4 nanotube	574 F g^{-1} at 0.1 A g^{-1}	5% loss after 1000 cycles	40
Porous cobalt oxides	219 F g^{-1} at 0.2 A g^{-1}	5% loss after cycles	41
Co_3O_4/SWCNT	313.9 F g^{-1} at 1 A g^{-1}	20% loss after 3000 cycles	42
Poly pyrrole/cobalt oxide composite	409 F g^{-1} at 0.2 A g^{-1}	Negligible amount of capacitance loss after 1000 cycles	43
Co_3O_4/MWCNT electrode/PANI	382 F g^{-1} at 1 A g^{-1}	NA	44
Co_3O_4/PPy core shell	2.11 F cm^{-1} at 2 mA g^{-1}	15.5% loss after 5000 cycles	45
Co_3O_4/rGO electrode	2272 mF cm^{-2} at 5 mA cm^{-2}	19.4% loss after 2000 cycles	46
Co_3O_4@MWCNT/polyindole	442.5 F g^{-1} at 1 A g^{-1}	9.8% loss after 5000 cycles	47
Co_3O_4@MWCNT/polypyrrole	609 F g^{-1} at 3 A g^{-1}	2.5% loss after 5000 cycles	Present study

[a] NA-not applicable.

the variation of specific capacitance for 5000 cycles. The hybrid composite electrode exhibits good stability and reversibility, with cycling efficiency of 97.1% after 5000 cycles. The energy and power density (Fig. 4(f)) of the hybrid electrode show 84.58, 67.08, 50.55, 40.44, and 36.25 (W h kg^{-1}), and 1,500, 3,450, 5,056, 6,330, and 7636 (W kg^{-1}), corresponding to 3, 7, 10, 13, and 15 A g^{-1}, respectively. It is critical for supercapacitors to maintain large capacitances under high charge/discharge current densities, as they may use potential hybrid electrodes for supercapacitor applications.[36–45] Table 1 shows that we also compared our results with the previously reported MWCNT/Co_3O_4 and conducting polymer cobalt oxide hybrid composite electrodes.

3.8. Electrochemical impedance spectroscopy (EIS) analysis

Fig. 4(e) shows the typical Nyquist plots of the hybrid electrode. The plot consists of a semicircle at the high frequency region, and a straight line at the low frequency region. From the point intersecting with the real axis in the range of high frequency, the internal resistance of the hybrid composite electrode in an open circuit condition is evaluated, which is composed of three sections:[35,36] the ionic resistance of the electrolyte, the intrinsic resistance of the electro active material, and the contact resistance between the active material and the current collector. In the high-to-medium frequency region, one semicircle related to faradic reactions can be discovered, which should be attributed to the charge transfer resistance at the electrode/electrolyte interface.[35,36] The low ESR value and comparatively straight line in the low-frequency region may be due to the incorporation of Co_3O_4 hybrid composite, which enhanced the electrochemical properties of MWCNT/PPy. The charge transfer resistances (from the diameter of the semicircle) of the electrode before and after 1000 cycles were calculated to be 0.28 and 0.30 Ω, respectively, demonstrating the stable electrochemical performance of the material. The phase angle for the impedance plot of the active electrode was observed to be higher than 45° in the low frequencies, suggesting that the electrochemical capacitive behavior of the active electrode is not controlled by the diffusion process. These findings imply that the unique structure of the active electrode can facilitate ionic motion in the solid electrode.

4. Conclusions

In summary, nanocrystalline Co_3O_4/MWCNT/polypyrrole hybrid composites were synthesized *via* a hydrothermal reaction process, and their electrochemical properties were investigated by cyclic volumetric analysis. It has been shown that the hydrothermal reaction time has a significant influence on the hydrolysis rate, on nucleation, as well as polycrystalline behavior. The structural and morphological properties of the hybrid composite were characterized by XRD, and FE-TEM analysis. The XRD and FE-TEM analyses show that the spinal phase Co_3O_4 has been synthesized in the controlled nanometer scale. These results indicate that the Co_3O_4/MWCNT decorated and was homogeneously distributed between the PPy polymers. The preparation of the Co_3O_4/MWCNT composite *via* high-temperature calcination leads to the formation of hybrid structure. Therefore, the hybrid composite shows high electrochemical performance. The high cyclic stability, losing only 2.9% of its initial capacitance after 5000 cycles, indicates that the hybrid composite could be a potential candidate in the field of supercapacitors. To conclude, Co_3O_4/MWCNT/PPy hybrid composite electrodes were fabricated by a simple and cheap method, and proved to be promising for anodic electrodes for the electrochemical high-performance supercapacitor. This study shows promising potential for the fabrication of stable, cost-effective, and high-performance hybrid composite electrodes for supercapacitor applications.

Acknowledgements

This research was supported by the Basic Science Research Program through the National Research Foundation of Korea (NRF-2017R1D1A1B0328368), funded by the Ministry of Education; and also supported by "the Technology Innovation Industrial Program" (10051977, 30W/mm Super Thermal Nanoceramic Adhesive Material for Fuel efficiency of EV/HEV), funded by the Ministry of Trade, Industry & Energy (MI, Korea). Partial funding was supported by a grant for the Endowment Project of "Infrastructure Establishment of Thermal Energy Conversion and Desalination using Seawater Thermal Energy (2/3)", funded by the Korea Research Institute of Ships and Ocean Engineering (PES9060) and also supported by a grant from KEPCO Research Center (KEPRI) (Project: Development of ternary based refrigerant and waste heat recovery ORC cycle) and supported under the framework of 2017 International Cooperation Program managed by National Research Foundation of Korea (Grant No: 2017K1A4A3013662).

References

1 X. Lu, M. Yu, G. Wang, Y. Tong and Y. Li, *Energy Environ. Sci.*, 2014, **7**, 2160–2181.
2 P. Yang and W. Mai, *Nano Energy*, 2014, **8**, 274–290.
3 G. Huang, C. Hou, Y. Shao, B. Zhu, B. Jia, H. Wang, Q. Zhang and Y. Li, *Nano Energy*, 2015, **12**, 26–32.
4 G. Wang, L. Zhang and J. Zhang, *Chem. Soc. Rev.*, 2012, **41**, 797–828.
5 L. L. Zhang and X. Zhao, *Chem. Soc. Rev.*, 2009, **38**, 2520–2531.
6 Y. Liu, H. H. Wang, J. Zhou, L. Y. Bian, E. W. Zhu, J. F. Hai, J. Tang and W. H. Tang, *Electrochim. Acta*, 2013, **112**, 44–52.
7 T. I. Schnoor, G. Smith, D. Eder, K. K. Koziol, G. T. Burstein, A. H. Windle and K. Schulte, *Carbon*, 2013, **60**, 229–235.
8 P. Simon and Y. Gogotsi, *Nat. Mater.*, 2008, **7**, 845–854.
9 C. H. Kim and B. H. Kim, *J. Power Sources*, 2015, **274**, 512–520.
10 P. Simon and Y. Gogotsi, *Nat. Mater.*, 2008, **7**, 845–854.
11 W. K. Jang, J. Yun, H. I. Kim and Y. S. Lee, *Carbon Lett.*, 2011, **12**, 162–166.
12 P. Liu, X. Wang and H. D. Li, *Synth. Met.*, 2013, **181**, 72–78.
13 R. P. Mahore, D. K. Burghate and S. B. Kondawar, *Adv. Mater. Lett.*, 2014, **5**, 400–405.

14 T. Zhu, J. S. Chen and X. W. Lou, *J. Mater. Chem.*, 2010, **20**, 7015–7020.
15 X. C. Dong, H. Xu, X. W. Wang, *et al.*, *ACS Nano*, 2012, **6**, 3206–3213.
16 G. He, J. Li, H. Chen, *et al.*, *Mater. Lett.*, 2012, **82**, 61–63.
17 Y. Y. Liang, M. G. Schwab, L. G. Zhi, E. Mugnaioli, U. Kolb, X. L. Feng and K. Mullen, *J. Am. Chem. Soc.*, 2010, **132**, 15030–15037.
18 Y. Zhang, H. Feng, X. Wu, L. Wang, A. Zhang, T. Xia, *et al.*, *Int. J. Hydrogen Energy*, 2009, **34**, 4889–4899.
19 S. Xiong, C. Yuan, X. Zhang, *et al.*, *J. Mater. Chem.*, 2009, **15**, 5320–5326.
20 P. Manivel, S. Kanagaraj, A. Balamurugan, N. Ponpandian, D. Mangalaraj and C. Viswanathan, *Colloids Surf., A*, 2014, **441**, 614–622.
21 S. R. Sivakkumar, J. M. Ko, D. K. Kim, *et al.*, *Electrochim. Acta*, 2007, **52**, 7377–7385.
22 C. Johne, R. Fritzsch and A. Ignaszak, *Electroanalysis*, 2014, **26**, 1560–1566.
23 R. Zhou, C. Meng, F. Zhu, *et al.*, *Nanotechnology*, 2010, **21**, 345701–345707.
24 Q. Y. Li, Z. S. Li, L. Lin, *et al.*, *Chem. Eng. J.*, 2010, **156**, 500–504.
25 S. Paul, Y. S. Lee, J. A. Choi, Y. C. Kang and D. W. Kim, *Bull. Korean Chem. Soc.*, 2010, **31**(5), 1228–1232.
26 M. Setka, J. Drbohlavova and J. Hubalek, *Sensors*, 2017, **17**, 562–580.
27 B. Zhang, Y. Xu, Y. Zheng, L. Dai, M. Zhang, J. Yang, Y. Chen, X. Chen and J. Zhou, *Nanoscale Res. Lett.*, 2016, **201**(6), 431–436.
28 X. Wang, S. Liu, H. Wang, F. Tu, D. Fang and Y. Li, *J. Solid State Electrochem.*, 2012, **16**, 113593–113602.
29 T. Zhu, J. S. Chen and X. W. Lou, *J. Mater. Chem.*, 2010, **20**, 7015–7020.
30 G. X. Wang, X. P. Shen, J. Horvat, B. Wang, H. Liu, D. Wexler and J. Yao, *J. Phys. Chem. C*, 2009, **113**, 4357–4361.
31 J. Yan, T. Wei, W. Qiao, B. Shao, Q. Zhao, L. Zhang and Z. Fan, *Electrochim. Acta*, 2010, **55**, 6973–6978.
32 M. Sevilla and R. Mokaya, *Energy Environ. Sci.*, 2014, **7**, 1250–1280.
33 L. Tao, L. Shengjun, Z. Bowen, W. Bei, N. Dayong, C. Zeng, Y. Ying, W. Ning and Z. Weifeng, *Nanoscale Res. Lett.*, 2015, **10**, 208–215.
34 J. Oh, M. E. Kozlov, B. Kim, H. K. Kim, R. H. Baughman and Y. H. Hwang, *Synth. Met.*, 2008, **158**, 638–641.
35 H. D. Abruna, Y. Kiya and J. C. Henderson, *Phys. Today*, 2008, **6**, 43–47.
36 Y. Wang and Y. Xia, *Adv. Mater.*, 2013, **25**, 5336–5342.
37 B. E. Conway and W. G. Pell, *J. Solid State Electrochem.*, 2003, **7**, 637–644.
38 H. Wei, J. Zhu, S. Wu, *et al.*, *Polymer*, 2013, **54**, 1820–1831.
39 S. G. Kandalkar, D. S. Dhawale, C.-K. Kim and C. D. Lokhande, *Synth. Met.*, 2010, **160**, 1299–1302.
40 J. Xu, L. Gao, J. Cao, W. Wang and Z. Chen, *Electrochim. Acta*, 2010, **56**, 732–736.
41 J. P. Cheng, X. Chen, J.-S. Wu, F. Liu, X. B. Zhang and V. P. Dravid, *CrystEngComm*, 2012, **14**, 6702–6709.
42 N. Iqbal, X. Wang, J. Ge, J. Yu, H. Y. Kim, S. S. Al-Deyab, M. El-Newehyf and B. Ding, *RSC Adv.*, 2016, **6**, 52171–52179.
43 H. Wei, C. He, J. Liu, H. Gu, Y. Wang, X. Yan, J. Guo, D. Ding, N. Z. Shen, X. Wang and S. W. Z. Guo, *Polymer*, 2015, **67**, 192–199.
44 R. Bushra, T. Arfin, M. Oves, W. Raza, F. Mohammad, M. A. Khan, A. Ahmad, A. Azam and M. Muneer, *New J. Chem.*, 2016, **40**, 9448–9459.
45 X. Yang, K. Xu, R. Zou and J. Hu, *Nano-Micro Lett.*, 2016, **8**, 143–150.
46 S. Wang, P. Ju, Z. Zhu and C. Zhao, *RSC Adv.*, 2016, **6**, 99640–99647.
47 X. Zhou, A. Wang, Y. Pan, C. Yu, Y. Zou, Y. Zhou, Q. Chen and S. Wu, *J. Mater. Chem. A*, 2015, **3**, 13011–13015.